GEOPHYSICS, VOL. 80, NO. 1 (JANUARY-FEBRUARY 2015); P. D75–D88, 19 FIGS., 4 TABLES.
10.1190/GEO2014-0196.1

Investigation of borehole cross-dipole flexural dispersion crossover through numerical modeling

Xinding Fang[1], Arthur Cheng[2], and Michael C. Fehler[1]

ABSTRACT

Crossover of the dispersion of flexural waves recorded in borehole cross-dipole measurements is interpreted as an indicator of stress-induced anisotropy around a circular borehole in formations that are isotropic in the absence of stresses. We have investigated different factors that influence flexural wave dispersion. Through numerical modeling, we determined that for a circular borehole surrounded by an isotropic formation that is subjected to an anisotropic stress field, the dipole flexural dispersion crossover is detectable only when the formation is very compliant. This might happen only in the shallow subsurface or in zones having high pore pressure. However, we found that dipole dispersion crossover can also result from the combined effect of formation intrinsic anisotropy and borehole elongation. We found that a small elongation on the wellbore and very weak intrinsic anisotropy can result in a resolvable crossover in flexural dispersion that might be erroneously interpreted as borehole stress-induced anisotropy. A thorough and correct interpretation of flexural dispersion crossover thus has to take into account the effects of stress-induced and intrinsic anisotropy and borehole cross-sectional geometry.

INTRODUCTION

Borehole sonic logging measurements provide important information about subsurface rock elasticity (Mao, 1987; Sinha and Kostek, 1995). Monopole and cross-dipole sonic logs are widely used for determining formation P- and S-wave velocities and shear anisotropy (Sinha and Kostek, 1995, 1996; Winkler et al., 1998; Tang et al., 1999, 2002; Fang et al. 2013a). Drilling a borehole in a formation strongly alters the stress distribution (Amadei, 1983; Gaede et al., 2012) in its vicinity that can affect formation elasticity and lead to stress-induced anisotropy around the borehole when in situ stresses are anisotropic (Sinha and Kostek, 1996; Winkler, 1996; Winkler et al., 1998; Tang et al., 1999; Fang et al., 2013b). Drilling-induced stress variations may also change borehole cross-sectional geometry due to rock failure, e.g., breakouts, when the concentrated stress around the borehole exceeds the rock strength (Zoback et al., 1985; Sayers et al., 2008). The borehole stress-induced anisotropy and cross-sectional geometry change due to the drilling-induced stress redistribution affect borehole sonic wave propagation (Fang and Fehler, 2014a, 2014b); thus, velocity estimated from borehole sonic logs might be biased from that of the virgin formation. Therefore, achieving a correct interpretation of sonic measurements requires an understanding of the relationship between the stresses and the elastic and inelastic responses of the formation around a borehole.

Sinha and Kostek (1996) study the effect of tectonic stresses on borehole acoustic-wave velocity by using the third-order elastic constants to account for the variations of elastic properties associated with the finite deformation caused by tectonic stresses. Later, Liu and Sinha (2000, 2003) study the influence of borehole stress concentration on monopole and dipole dispersion curves by using 2.5D and 3D finite-difference methods to solve the elastic-wave equation and the nonlinear constitutive relation determined by the third-order elastic constants. Tang et al. (1999) use an empirical stress-velocity coupling relation to estimate the variation of shear elastic constants as a function of stresses around a borehole. Sayers (2005, 2007) and Sayers et al. (2007, 2008) study the elastic and inelastic effects of borehole stress concentration on elastic-wave velocities in sandstones using a nonlinear grain boundary compliance model. Brown and Cheng (2007) and Fang et al. (2013b) propose to calculate the borehole stress-induced anisotropy by, respectively, using the fabric tensor model (Oda et al., 1986) and the model of Mavko et al. (1995) to describe the stress-dependent elastic response of microcracks embedded in rocks. Fang et al.

Manuscript received by the Editor 25 April 2014; revised manuscript received 29 September 2014; published online 22 December 2014.
[1]Massachusetts Institute of Technology, Department of Earth, Atmospheric and Planetary Sciences, Cambridge, Massachusetts, USA. E-mail: xinfang@mit.edu; fehler@mit.edu.
[2]Formerly Halliburton, Houston, Texas, USA; presently National University of Singapore, Singapore. E-mail: arthurcheng@alum.mit.edu.

(2013b) use a method that includes the coupling between the stress and stress-induced anisotropy, whereas previous investigations assumed that stress is that given in a prestressed isotropic rock. Fang et al. (2014) use 2D and 3D finite-difference methods to investigate the influence of borehole stress-induced anisotropy on borehole compressional wave propagation. All these studies conclude that borehole stress-induced formation stiffness changes have substantial impact on borehole sonic logging measurements. Here, we focus on studying the effect of stresses on borehole dipole flexural wave propagation.

Sinha and Kostek (1996) find that formation anisotropic stresses cause radially varying heterogeneities in acoustic-wave velocities that vary with azimuth relative to the two principal stresses perpendicular to the wellbore and can result in a crossover in cross-dipole flexural dispersion curves, in which the azimuthal orientations of fast and slow waves differ between low and high frequencies. This flexural dispersion crossover has long been taken to be an indicator of borehole stress-induced anisotropy because the crossover cannot occur for a circular borehole located in a homogeneous anisotropic formation (Sinha and Kostek, 1996; Sinha et al., 2000). Sinha (2001), Sinha and Liu (2002; 2004) and Liu and Sinha (2003) study the influence of small uniaxial and triaxial stresses on the flexural dispersion and confirm the existence of flexural dispersion crossover caused by borehole stress alteration. Although the azimuthal dependence of flexural dispersion for a vertical borehole is related to the differential stress (i.e., $S_H - S_h$) that induces an azimuthal variation in hoop stress around a borehole, the variation in rock properties with stress decreases as overall background stress increases. Thus, it is important to investigate the borehole dipole response under the compression of triaxial stresses with different magnitudes.

Splitting of dipole flexural waves into fast and slow components can be caused by borehole stress-induced anisotropy; formation intrinsic anisotropy caused by aligned geologic structures, such as bedding, microstructures, or fractures; noncircular borehole cross sections (Simsek et al., 2007; Simsek and Sinha, 2008a, 2008b); and drilling-induced fractures (Zheng et al., 2009, 2010; Lei and Sinha, 2013). If we consider their effects separately, borehole stress-induced anisotropy is usually taken to be the cause of the flexural dispersion crossover because the influence of borehole stress-induced anisotropy on flexural wave velocity differs between low and high frequencies and it varies with azimuthal location on the borehole. Zheng et al. (2010) show that a deep drilling-induced solid-filled fracture on the wellbore can also cause a crossover in dipole dispersion. However, these factors may occur together in the earth and affect sonic wave propagation simultaneously. In this paper, we will investigate the influence of the first three factors, although we do not consider the drilling-induced fractures, which is beyond the scope of this paper. We will briefly discuss the effect of drilling-induced fractures in the "Discussion" section.

Velocities of low-frequency flexural waves approach the velocity of the virgin formation, whereas velocities of high-frequency waves are more sensitive to the near-borehole environment including the cross-sectional geometry and borehole stress-induced anisotropy. We will show that when the formation exhibits transversely isotropic anisotropy and its symmetry axis is in a close alignment with the short dimension (for a fast formation) or elongation dimension (for a slow formation) of a noncircular borehole cross-section, a crossover in flexural dispersion might occur. We first simulate the effect of stress-induced anisotropy on dipole flexural wave dispersion and compare the results for uniaxial and triaxial stress conditions. We then model the combined effect of intrinsic anisotropy and borehole elongation on flexural wave dispersion and show that there is another possible interpretation of flexural dispersion crossover.

EFFECT OF STRESS-INDUCED ANISOTROPY ON FLEXURAL DISPERSION

Modeling borehole stress-induced anisotropy

To model the effect of borehole stress concentration on the elasticity of the formation around a borehole, we use the method of Fang et al. (2013b) to calculate the stress-dependent stiffness of the formation around a borehole for a given stress state. Following Mavko et al. (1995), we use laboratory-measured P- and S-wave velocities versus hydrostatic pressure data to calculate the stress-dependent rock stiffness tensor of a given rock sample that is taken to represent the formation rock around the borehole. We then iteratively calculate the stress distribution around the borehole using a finite-element method and subsequently update the model stiffness tensor, which is a function of space due to the spatially varying stress. When the iteration converges, the output from this approach is the stiffness tensor (21 elastic constants) of the model as a function of space and applied stress. The accuracy of this modeling approach has been validated through comparison with the stress-strain and the acoustic data measured in laboratory borehole experiments under uniaxial stress compression (Fang et al., 2013b, 2014). This is a purely elastic method, so we neglect the effect of rock failure. Also, the effect of stress-induced crack opening is not considered. Crack opening is important when the hoop stress becomes tensile, which generally occurs when $S_H > 3S_h$ (Fang et al., 2013b). This method provides a means to obtain an anisotropic elastic model that accounts for the presence of a borehole and the constitutive relation between an in situ stress field and the stiffness tensor for a rock, which is essential for correctly predicting the borehole acoustic response in sonic logging measurements (Fang et al., 2014).

We use the velocity versus pressure data for four different rock samples measured by Coyner (1984) to construct borehole models for four different formation rocks. Velocities of all samples are assumed to be isotropic under hydrostatic compression. Figure 1 shows the P- and S-wave velocities (solid and open squares) together with the shear moduli (blue triangles) calculated from the S-wave velocity of the four rock samples measured at different effective pressures. These measurements were conducted under water saturation and with a constant 10 MPa pore pressure applied. Table 1 lists the density, porosity, and grain size of the rock samples. Density is assumed to be stress independent because the change of density caused by stress loading is negligible (Coyner, 1984). Velocities of the three sandstone samples increase significantly at low effective pressures, and the changes in velocity become smaller as pressure increases due to the closing of microcracks/pores in the rocks under compression. Velocities of the Bedford limestone sample are weakly dependent on pressure, suggesting that this rock sample is very stiff because it has low porosity and a large grain size (see Table 1). Generally, the change of shear modulus with pressure is more rapid when the pressure is below about 20 MPa, beyond which the variation in shear modulus becomes smaller.

The velocity versus pressure data in Figure 1 are taken as our input to the method of Fang et al. (2013b) to build the elastic borehole models for the subsequent acoustic simulations. To avoid the model boundary effect in the finite-element calculation of model stress and stiffness in the method of Fang et al. (2013b), we set the x- and y-dimensions of the model region to be 4 m (borehole at center). The z-dimension is not considered in the finite-element calculation because the plain strain assumption is applied. A 3D staggered-grid finite-difference method (Cheng et al., 1995) with fourth-order accuracy in space and second-order accuracy in time is used in the wave propagation simulation. In all of the following simulations, the grid size is 2.5 mm and the time sampling is 25 μs. Validations of the finite-element and finite-difference programs are presented in Fang et al. (2014). Figure 2 is a schematic showing the borehole model geometry. The borehole radius is 10 cm, and the borehole axis is along the z-direction. The maximum horizontal stress S_H, minimum horizontal stress S_h, and vertical stress S_V are along the x-, y- and z-directions, respectively. Because the three principal stresses are aligned parallel and perpendicular to the borehole axis, the stress-induced anisotropy exhibits orthorhombic symmetry. The magnitude of the nine elastic constants C_{11}, C_{12}, C_{13}, C_{22}, C_{23}, C_{33}, C_{44}, C_{55}, and C_{66} is much larger than that of the other components of the stiffness tensor, and they dominate the wave propagation in the borehole (Fang et al., 2014). Thus, we only use the nine dominant components and assume that the other components in the stiffness tensor are equal to zero in the finite-difference simulations below. For the wave propagation simulation, we use a dipole source (red circle in Figure 2) with a 3-kHz Ricker wavelet. A receiver array extending along the z-direction is 5 cm away from the borehole center in the dipole inline direction. The first receiver is 2 m above the source in the z-direction and an additional 50 receivers with 4 cm spacing are positioned at distances between 2 and 4 m. To avoid aliasing in the dispersion analysis, the receiver array used in the simulation is much denser than that in a real sonic tool. A perfectly matching layer absorbing boundary condition is added to all boundaries of the model.

Stresses around a borehole

Under the plane strain assumption, the stress around a circular borehole in an isotropic medium that is subjected to the compression of principal stresses S_H, S_h, and S_V, as shown in Figure 2, in cylindrical coordinates with radius r and azimuth θ measured relative to the maximum horizontal stress (S_H) direction is given as (e.g., Tang and Cheng, 2004)

$$\sigma = \begin{bmatrix} \sigma_{rr} & \sigma_{r\theta} & 0 \\ \sigma_{r\theta} & \sigma_{\theta\theta} & 0 \\ 0 & 0 & \sigma_{zz} \end{bmatrix}, \quad (1)$$

with

$$\begin{aligned}
\sigma_{rr} &= \frac{1}{2}(S_H + S_h)\left(1 - \frac{a^2}{r^2}\right) \\
&\quad + \frac{1}{2}(S_H - S_h)\left(1 - \frac{4a^2}{r^2} + \frac{3a^4}{r^4}\right)\cos 2\theta, \\
\sigma_{\theta\theta} &= \frac{1}{2}(S_H + S_h)\left(1 + \frac{a^2}{r^2}\right) \\
&\quad - \frac{1}{2}(S_H - S_h)\left(1 + \frac{3a^4}{r^4}\right)\cos 2\theta, \\
\sigma_{r\theta} &= -\frac{1}{2}(S_H - S_h)\left(1 + \frac{2a^2}{r^2} - \frac{3a^4}{r^4}\right)\sin 2\theta, \\
\sigma_{zz} &= S_V + \nu(\sigma_{rr} + \sigma_{\theta\theta}), \quad (2)
\end{aligned}$$

where a is the borehole radius and ν is Poisson's ratio. We assume that the wellbore is permeable and the borehole fluid pressure is

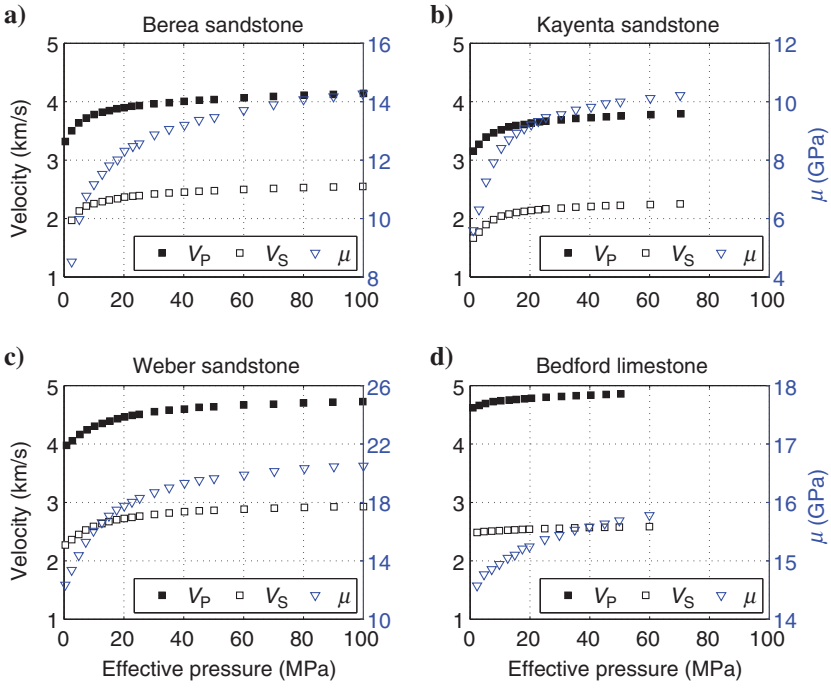

Figure 1. P- (solid squares) and S-wave (open squares) velocities together with the shear moduli μ (blue triangles) calculated from S-wave velocity for four different rock samples versus confining effective pressure (modified from Coyner, 1984).

Table 1. Properties of four rock samples (from Coyner, 1984).

Rock	Density	Porosity	Grain size
Berea sandstone	2197 kg/m^3	17.8%	0.1 mm
Kayenta sandstone	2017 kg/m^3	22.2%	0.15 mm
Weber sandstone	2392 kg/m^3	9.5%	0.05 mm
Bedford limestone	2360 kg/m^3	11.9%	0.75 mm

equal to pore pressure, so we only consider effective stress in our study.

Following Sinha et al. (2000), we decompose the stress field into a reference confining stress S_V and deviatoric stresses $S_H - S_V$ and $S_h - S_V$, as shown in Figure 3, to analyze the effect of in situ stresses on borehole sonic wave propagation. When $S_H = S_h = S_V$, the terms containing $\cos 2\theta$ or $\sin 2\theta$ in equation 1 vanish and the stress tensor in equation 1 represents the stress state under hydrostatic compression. In previous studies of Sinha and Kostek (1996) and Tang et al. (1999), borehole stress-induced anisotropy is assumed to be caused by the deviatoric stresses that impose the azimuthally varying hoop stress near the wellbore, whereas the confining stress is assumed to only alter the whole model from the zero stress state to some hydrostatically loaded reference state that can be superposed on the biasing stress-induced changes. However, while confining stress does not cause azimuthal variation in the hoop stress, it is effective in stiffening a rock and making the deviatoric stresses less efficient in producing stress-induced anisotropy around a borehole. Previous modeling studies of borehole stress-induced anisotropy considered the situations of either uniaxial/biaxial stress compression (Sinha et al., 1995; Sinha and Kostek, 1996; Tang et al., 1999; Brown and Cheng, 2007; Fang et al., 2013b) or small triaxial stress compression (Sinha and Liu, 2002, 2004; Liu and Sinha, 2003). In laboratory experiments (Winkler, 1996; Winkler et al., 1998; Fang et al., 2013b), uniaxial stress is used to effectively represent the differential stress ($S_H - S_h$) that introduces the azimuthal variation terms in equations 1. A thorough analysis of the problem should consider the cases of small and large triaxial stresses that, respectively, represent the stress states in shallow and deep reservoirs. In the following, we first simulate models for the four rock types under uniaxial stress compression and then compare results for triaxial stress compression in which deviatoric stresses are superposed onto a varying confining stress.

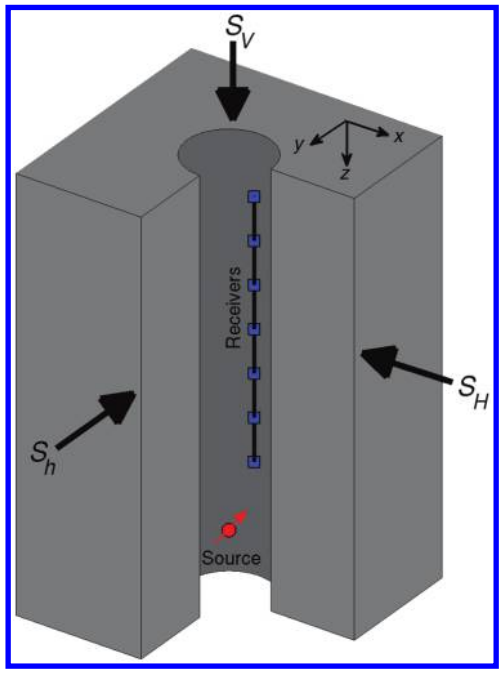

Figure 2. Schematic showing the borehole model under triaxial stress compression. Here, S_H, S_h, and S_V are along the x-, y-, and z-directions, respectively. The red circle and blue squares, respectively, represent the source and receivers in the borehole. The borehole radius is 10 cm. Dipole source is located at the center of the borehole. Receivers are 5 cm away from the borehole center along the dipole inline direction. The dipole orientation is measured from the positive x-direction.

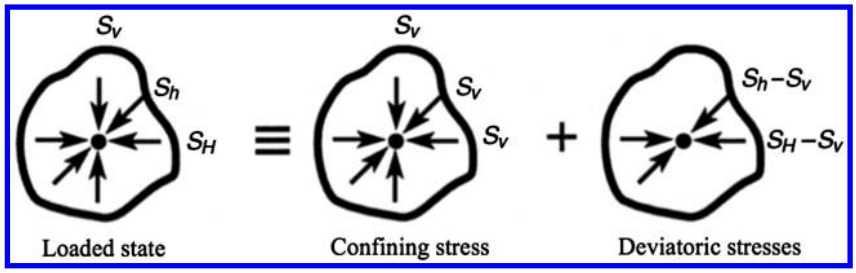

Figure 3. Decomposition of actual stresses (S_H, S_h, and S_V) into a confining stress S_V and biaxial deviatoric stresses $S_H - S_V$ and $S_h - S_V$ in the borehole cross-sectional plane (modified from Sinha et al., 2000).

Uniaxial stress compression

We first study the effect of uniaxial compression on dipole flexural wave propagation. Uniaxial stress (i.e., S_H) is applied normal to the borehole axis in the x-direction. Hereafter, stress always refers to effective stress, which is the difference between the loading stress and pore pressure, which is 10 MPa in the velocity measurements shown in Figure 1. Figure 4 shows the variations of the stiffness of the Berea sandstone borehole model when it is subjected to 10 MPa uniaxial stress compression in the x-direction. The large variations in the model stiffness near the wellbore are caused by the borehole stress alteration. Figure 5 shows the synthetic waveforms recorded in the borehole for dipoles at 0° (solid black traces) and 90° (dashed red traces). Note that 0° and 90° are, respectively, the directions along the x- and y-axes. The flexural dispersion at 0° and 90° is obtained by using the method of Rao and Toksöz (2005) to separately process the array waveforms for dipoles at the two azimuths. Figure 6 shows the cross-dipole flexural dispersion for models with four different formation rocks. We only show the dispersion within the frequency range of 2 to 7 kHz because the sources (3-kHz center frequency) have little energy at frequencies beyond 7 kHz. For Berea, Kayenta, and Weber sandstones, the dipole flexural dispersion curves clearly show crossovers between 4 and 5 kHz, whereas the two dispersion curves for Bedford limestone overlap with each other, making the crossover indistinguishable. These results indicate that we can expect to see the flexural dispersion crossover for compliant rocks under uniaxial stress compression. For stiff rocks, such as the Bedford limestone sample, the dispersion crossover is unresolvable because the two flexural dispersion curves are nearly identical. The flexural dispersion results under uniaxial compression are in agreement with the theoretical prediction of Sinha and Kostek (1996) and the laboratory results of Sinha et al. (1995) and Winkler et al. (1998).

Triaxial stress compression

Although confining stress does not cause azimuthal variation in the stress around a borehole, it is effective in stiffening a rock by closing the

microcracks and making the deviatoric stresses less efficient in producing stress-induced anisotropy around a borehole. The stiffening of rocks with increasing confining stress can be clearly seen in Figure 1. The closure of a crack is related to the normal traction applied at the crack surfaces (Mavko et al., 1995; Sayers, 2007). The normal component of the traction acting on a crack with unit normal $\mathbf{n}$ is given by

$$\sigma_n = \mathbf{n}^T \sigma \mathbf{n}, \tag{3}$$

where $\mathbf{n}^T$ is the transpose of $\mathbf{n}$.

For hydrostatic compression $S_H = S_h = S_V$, substituting equation 1 into equation 3, we have

$$\sigma_n = S_V(1 + 2\nu n_3^2) - S_V \frac{a^2}{r^2}[(\mathbf{n}\cdot\mathbf{e}_r)^2 - (\mathbf{n}\cdot\mathbf{e}_\theta)^2], \tag{4}$$

where $\mathbf{e}_r = [\cos\theta, \sin\theta, 0]^T$ and $\mathbf{e}_\theta = [-\sin\theta, \cos\theta, 0]^T$ are, respectively, the unit vectors in the radial and azimuthal directions, as shown in Figure 7, n_3 is the z-component of $\mathbf{n}$.

In equation 4, $\mathbf{n}\cdot\mathbf{e}_r$ and $\mathbf{n}\cdot\mathbf{e}_\theta$, respectively represent the projections of the crack normal in the radial and azimuthal directions. Cracks having $|\mathbf{n}\cdot\mathbf{e}_r| > |\mathbf{n}\cdot\mathbf{e}_\theta|$ affect the borehole flexural wave propagation more significantly because their planes are close to normal to the radial direction $\rightarrow \mathbf{e}_r$, which is the flexural wave polarization direction. If we assume that cracks are randomly distributed and those cracks with orientations satisfying $|\mathbf{n}\cdot\mathbf{e}_r| > |\mathbf{n}\cdot\mathbf{e}_\theta|$ have a dominant effect on flexural wave propagation, then confining stress makes the far-field formation stiffer compared with the near-field for flexural wave propagation because equation 4 shows that σ_n increases radially on cracks for which $|\mathbf{n}\cdot\mathbf{e}_r| > |\mathbf{n}\cdot\mathbf{e}_\theta|$. The radial dependence of σ_n suggests that the effect of hydrostatic stress on flexural wave velocity is frequency dependent. So the difference between the cross-dipole flexural dispersion curves is not solely determined by the differential stress $S_H - S_h$, but it also depends on the overburden stress S_V.

In our numerical modeling, we vary S_V from 5 to 30 MPa to simulate the change of overburden stress with depth while keeping the deviatoric stresses ΔS_H $(S_H - S_V)$ and ΔS_h $(S_h - S_V)$ at 5 and -5 MPa. Table 2 lists the values of stresses for four different stress states that we studied. The Mohr's circle representation of triaxial stress shown in Figure 8 illustrates the relationship among the stress states in Table 2. Increasing S_V while fixing ΔS_H and ΔS_h drives the Mohr's circle to move along the normal traction axis in the normal-shear traction coordinates, which results in the increase of normal traction on cracks of all orientations.

Figure 9 shows the radial variations of the shear modulus (e.g., C_{44} and C_{55} shown in Figure 4) in the radial planes at 0° and 90° for the four rock samples in four different triaxial stress states (Table 2). Solid and dashed curves, respectively, show the variations of C_{55} along the x-direction (0°) and C_{44} along the y-direction (90°). The black, red, blue, and magenta colors represent the results for $S_V = 5$, 10, 20, and 30 MPa, respectively. In Figure 9, we can see that the shear moduli of all rock samples exhibit similar radial variations. For all stress states, the shear modulus at 0° (solid curves) is larger than that at 90° (dashed curves) in the far-field ($r > 3a$), whereas this reverses in the near-field due to the borehole stress alteration. The shear moduli in the far-field asymptotically approach the values of an intact formation without the borehole under stress. Because low-frequency flexural waves probe deeper into the forma-

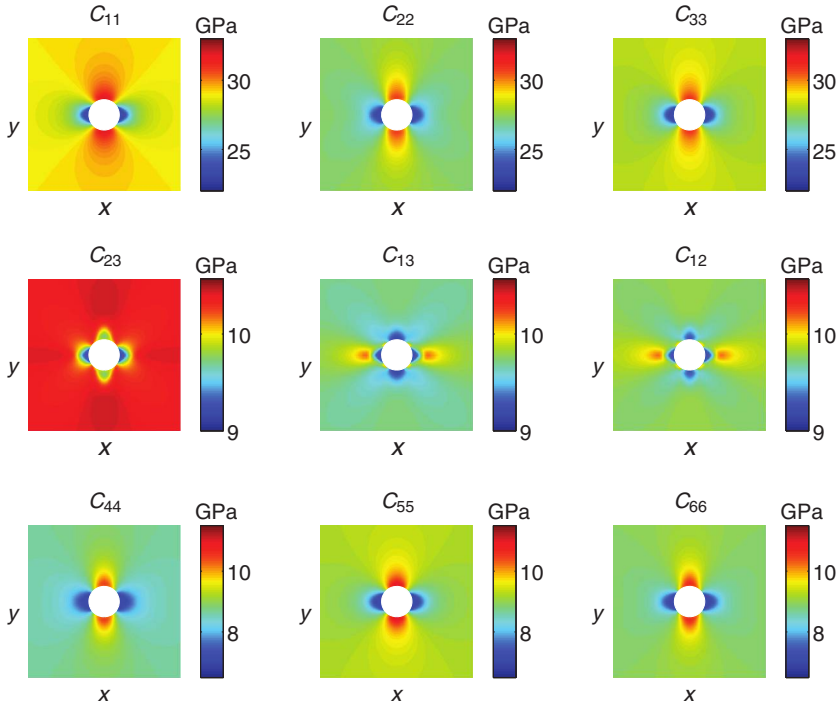

Figure 4. Variations of the stiffness of the Berea sandstone borehole model in the x-y-plane when a 10-MPa uniaxial stress is applied in the x-direction.

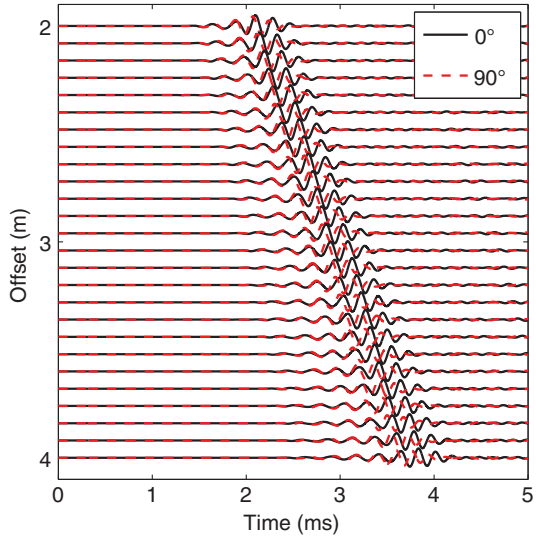

Figure 5. Synthetic traces from the Berea sandstone borehole model when it is subjected to 10 MPa uniaxial stress compression in the x-direction. Solid black and dashed red traces are the data for dipoles at 0° and 90°, respectively.

tion and high-frequency waves probe shallower, a crossover may occur in the dispersion curves of the cross-dipole. For a given confining stress, the difference between the shear moduli at the two azimuths is smaller in the far-field compared with that in the near-field. This indicates that low-frequency flexural waves have smaller azimuthal variation compared with the high-frequency waves. The merging of the solid and dashed curves with increasing confining stress S_V in the far-field suggests that the velocities of low-frequency flexural waves have little azimuthal dependence when the confining stress is large. Therefore, the presence of a nonzero confining stress adds a frequency-dependent shift to the flexural dispersion curves. We also observe that the variations of C_{44} along 90° (dashed curves) show corners near the wellbore for the cases of $S_V = 5$ and 10 MPa. This is caused by the radial variation of σ_{rr} along 90°. From equation 2, we have the radial stress along $\theta = 90^\circ$ as

$$\begin{aligned}\sigma_{rr}(\theta = 90^o) &= \frac{1}{2}(S_H + S_h)\left(1 - \frac{a^2}{r^2}\right) \\ &\quad - \frac{1}{2}(S_H - S_h)\left(1 - \frac{4a^2}{r^2} + \frac{3a^4}{r^4}\right) \\ &= S_h + \frac{(3S_H - 5S_h)^2}{24(S_H - S_h)} \\ &\quad - \frac{3}{2}(S_H - S_h)\left(\frac{a^2}{r^2} - \frac{3S_H - 5S_h}{6S_H - 6S_h}\right)^2. \quad (5)\end{aligned}$$

For the stress states with $S_V = 20$ and 30 MPa, σ_{rr} along 90° is monotonically increasing with radius r because of $3S_H \le 5S_h$. However, for the stress states with $S_V = 5$ and 10 MPa, σ_{rr} first increases then decreases with r and has a maximum value at $r = a\sqrt{\frac{6S_H - 6S_h}{3S_H - 5S_h}}$, whose value is between a and $2a$ for $S_V = 5$ and 10 MPa. Because the elastic properties are affected by the stress, the radial variation in σ_{rr} can result in a corner in the variation of C_{44} along 90°, as shown in Figure 9 for the cases of $S_V = 5$ and 10 MPa. The C_{55} along 0° behaves differently because the given stress states do not allow σ_{rr} to have a turning point along 0°.

Figure 10 shows the dispersion of cross-dipole flexural waves calculated from the synthetic waveforms for the three sandstone models in four different stress states (Table 2). The result for the Bedford limestone model is not shown here because it is too stiff to have a resolvable dispersion crossover. When $S_V = 5$ MPa, the two flexural dispersion curves for all three models are distinct and they intersect at about 4 to 5 kHz. However, for models with $S_V > 5$ MPa, the separation of the two flexural dispersion curves is so small that the dispersion crossover is hard to distinguish.

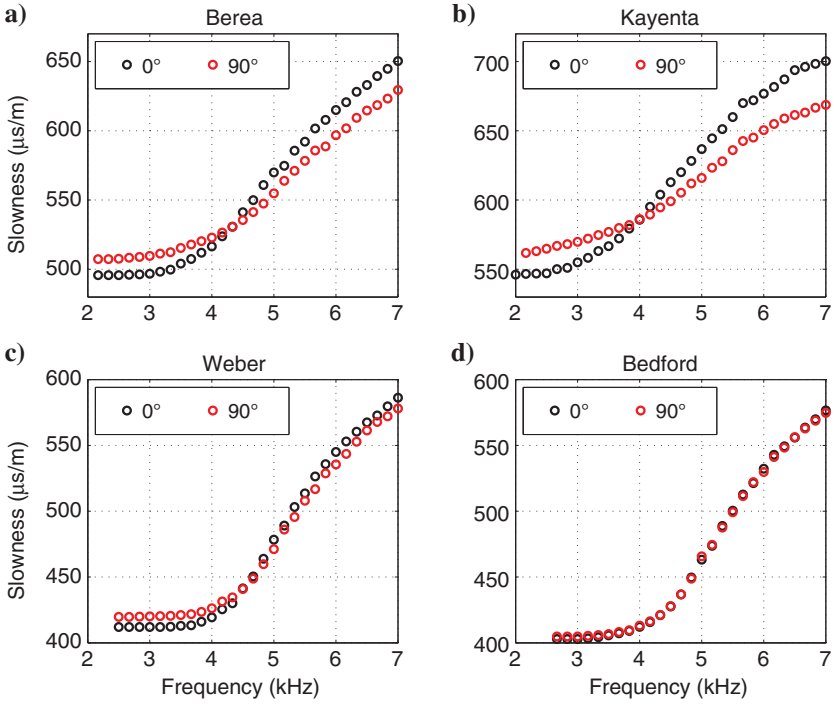

Figure 6. Flexural wave dispersion of the four rock samples under 10 MPa uniaxial stress applied along the x-direction. Black and red circles are, respectively the dispersion along the x- and y-directions (i.e., 0° and 90°, respectively).

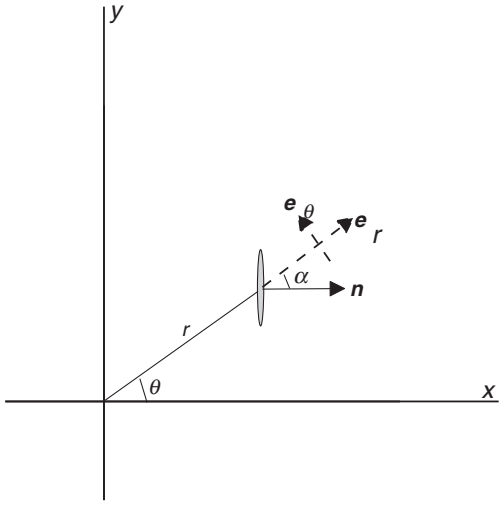

Figure 7. Schematic showing a microcrack at azimuth θ and at distance r from the origin with unit normal $\mathbf{n}$. Note that $\mathbf{e}_r$ and $\mathbf{e}_\theta$ are the unit vectors in the radial and azimuthal directions, respectively, and α is the angle between $\mathbf{n}$ and $\mathbf{e}_r$.

Table 2. Four different stress states in the triaxial compression simulations.

S_V	ΔS_H	ΔS_h	$S_H = S_V + \Delta S_H$	$S_h = S_V + \Delta S_h$
5 MPa	5 MPa	−5 MPa	10 MPa	0 MPa
10 MPa	5 MPa	−5 MPa	15 MPa	5 MPa
20 MPa	5 MPa	−5 MPa	25 MPa	15 MPa
30 MPa	5 MPa	−5 MPa	35 MPa	25 MPa

To show the dispersion difference, we calculate the difference by subtracting the dispersion data at 90° from those at 0°. Figure 11 shows the difference of the dispersion at the two azimuths in Figure 10. For $S_V = 5$, 10, and 20 MPa, the dispersion difference generally increases with frequency. The frequency at which there is zero difference (i.e., dispersion crossover frequency) occurs between 4 and 5 kHz and seems to be insensitive to the rock type and confining stress strength. When S_V goes up to 30 MPa, the two dispersion curves are almost identical and the crossover is indistinguishable. The precision of flexural wave slowness measured by a dipole sonic tool in the field is a few percent, for example 1% to 2% in a stiff limestone reservoir (Sinha et al., 2000). The dispersion difference shown in Figure 11 is less than 1% at most frequencies when $S_V \geq 10$ MPa, indicating that the flexural dispersion crossover is unresolvable in those cases. We only consider the case of $S_H > S_V > S_h$ in the modeling. The horizontal principal stresses may be less than, or greater than, the vertical stress, depending on the geologic setting (Zoback, 2010). If we increase S_V so that $S_V \geq S_H > S_h$ while keeping S_H and S_h unchanged, the results should be similar except that the overall difference between the dispersion curves becomes smaller because the change of S_V only affects the stress σ_{zz} in equation 1.

The results shown in Figures 10 and 11 indicate that the flexural dispersion crossover is hard to detect when a borehole is subjected to triaxial compression that contains a significantly large confining component. To better understand the relationship between stress and rock stiffness, we define the compressible compliance percentage of a rock as

$$\phi(p) = \frac{\mu^{-1}(p) - \mu_{\min}^{-1}}{\mu_{\max}^{-1} - \mu_{\min}^{-1}}, \tag{6}$$

where $\mu^{-1}(p)$ is the shear compliance (i.e., reciprocal of the shear modulus) at pressure p; $\mu_{\min}^{-1}$ and $\mu_{\max}^{-1}$, respectively, represent the minimum and maximum shear compliances of a rock when it is under the maximum and minimum pressures; and $\phi(p)$ represents the percentage of the remaining compressible compliance of a rock at pressure p with respect to the state at maximum loading pressure.

Figure 12 shows the compressible compliance percentage ϕ versus pressure for the four rock samples. We can see that ϕ decreases exponentially with pressure for all rock samples. For a given confining stress state, it is the remaining compressible compliance on which the biasing stresses can effect and cause the borehole stress-induced anisotropy. The change of rock stiffness caused by the deviatoric stresses decreases exponentially with the increase of confining stress because the compliance of the grain boundaries decreases exponentially with increasing stress (Sayers, 2007). Thus, a 10-MPa confining stress is sufficient to stiffen a rock to some state upon which the borehole stress-induced

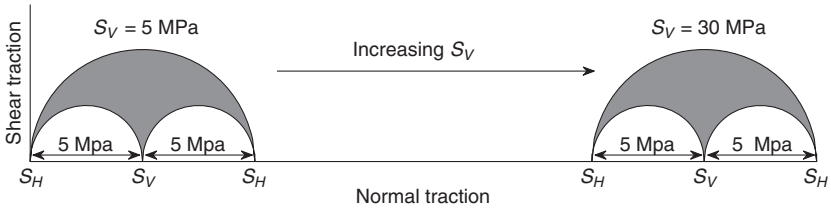

Figure 8. Mohr's circle representation of the changing of triaxial stress states in Table 2. The Mohr's circle horizontally shifts from left to right along the normal traction axis when the confining stress S_V increases.

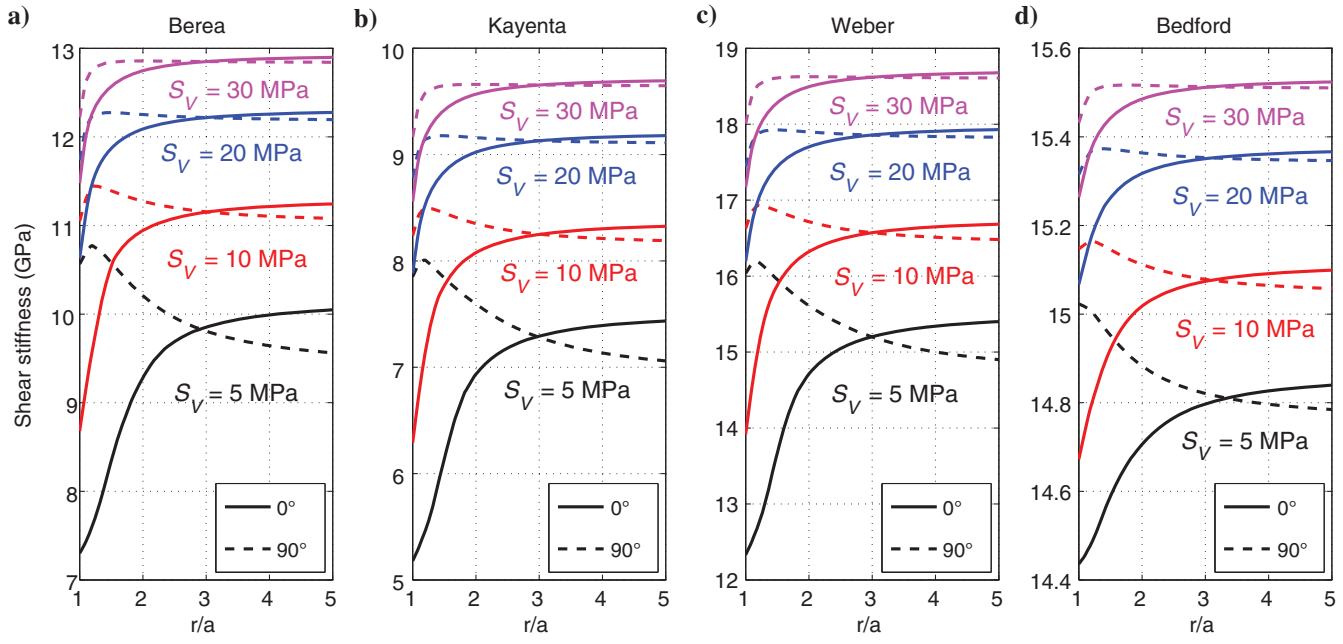

Figure 9. Radial variations of the shear moduli for the four rock samples under the compression of different triaxial stresses. Solid curves show the variations of C_{55} along the x (0°)-direction. Dashed curves show the variations of C_{44} along the y (90°)-direction. The black, red, blue, and magenta colors represent models under four different stress states that are listed in Table 2. Horizontal axes are the radial distance from borehole center normalized by the borehole radius a.

anisotropy caused by deviatoric stresses is too weak to separate the flexural dispersion curves, as shown in Figure 10.

From equation 2, we can see that the azimuthal variation of stress around a borehole increases with the increase of differential stress $\Delta S_{\text{Diff}} = S_H - S_h$, which was chosen to be constant for all stress states in Figure 10. To investigate whether an increase in differential stress can make the dispersion crossover distinguishable when a large confining stress is present, we change the value of S_h from 25 to 15 MPa while keeping S_H and S_V at 35 and 30 MPa, respectively, to generate three stress states with different differential stresses, as listed in Table 3. Figure 13a–13c shows the flexural dispersion for the Berea sandstone borehole model in three different stress states (Table 3) with the differential stress (ΔS_{Diff}) varying from 10 to 20 MPa. The dispersion differences shown in Figure 13d–13f are all below the resolution limit for measuring flexural slowness in field data, implying that the dispersion crossover will be unresolvable even in a case in which the differential stress is increased by two times. This comparison indicates that an increase in differential stress has little effect on separating the flexural dispersion curves when a rock is already stiffened by a large confining stress.

Through comparing the results for uniaxial and triaxial stress compressions, we can see that flexural dispersion under triaxial stress compression is different from that under uniaxial stress compression because the overburden stress S_V significantly influences the flexural wave behavior by stiffening a rock and reducing the flexural wave splitting. This suggests that the flexural dispersion crossover may be detectable only in the shallow subsurface or in high pore pressure zones with small effective confining pressure when a sufficiently strong differential stress is present.

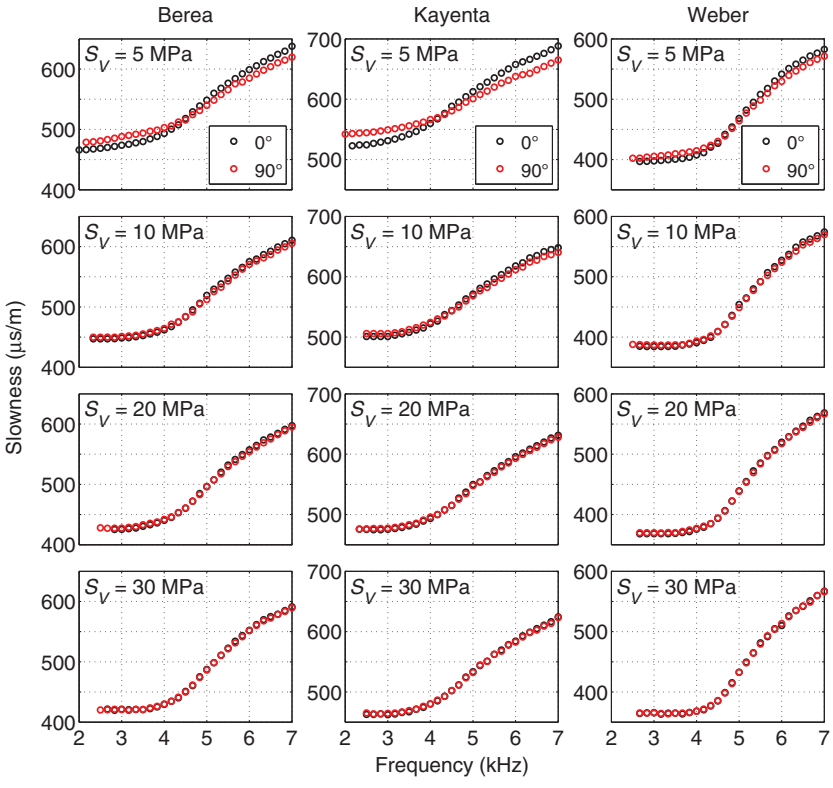

Figure 10. Flexural dispersion for three sandstone samples in four different triaxial stress states (Table 2). The vertical stress S_V is shown in each panel, the corresponding horizontal stresses are $S_H = S_V + 5$ MPa, $S_h = S_V - 5$ MPa. Black and red circles are, respectively, the dispersion along the x- and y-directions (0° and 90°, respectively).

EFFECT OF INTRINSIC ANISOTROPY AND BOREHOLE ELONGATION ON FLEXURAL DISPERSION

In the previous section, we discussed the flexural dispersion crossover caused by borehole stress-induced anisotropy. In this section, we will show that the flexural dispersion crossover can also result from the combined effect of formation intrinsic anisotropy and borehole elongation.

The approach of Fang et al. (2013b) used in the previous section for calculating the borehole stress-induced anisotropy has a basic assumption that a rock is isotropic at a zero stress state and elasticity anisotropy is caused by the closing of the compliant parts of the pore space due to tectonic stresses. Elasticity anisotropy in rocks includes intrinsic and stress-induced components (Jaeger et al., 2007). It is well recognized that most sedimentary rocks exhibit some degree of anisotropy, either stress-induced or intrinsic, or both. In contrast to stress-induced anisotropy, intrinsic anisotropy is caused by aligned geologic structures, such as bedding, microstructure, or fractures. To analyze the effect of intrinsic anisotropy on borehole flexural wave propagation, we assume that the formation around a borehole exhibits transversely isotropic anisotropy with the symmetry axis along the y-direction (i.e., HTI symmetry). To simplify the discussion in the following analysis, we only consider anisotropy with the Thomsen anisotropic parameters $\varepsilon = \gamma$ and $\delta = 0$. Because flexural wave propagation is mainly sensitive to the formation shear moduli (Tang and Cheng, 2004), the flexural wave dispersion behavior is mostly affected by the anisotropic parameter γ.

For a circular borehole in an HTI formation with the symmetry axis normal to the borehole axis and with no stress-induced anisotropy, dipole flexural waves split into fast and slow waves whose dispersion curves separate at low frequencies (e.g., they approach the equivalent formation slowness) while gradually merging toward each other at high frequencies (e.g., strongly influenced by borehole fluid); thus, they do not exhibit a crossover (Sinha et al., 2000). However, boreholes drilled in the earth are often noncircular. Noncircular borehole cross-sections may be caused by mechanical action of the drillstring in horizontal and deviated wells, by wellbore breakouts, and by severe washing out of the borehole in soft or poorly consolidated rocks (Sinha et al., 2000). Borehole cross-section geometry change due to wellbore elastic deformation under stress is negligible (see Appendix A for a demonstration). Asymmetry of noncircular borehole cross sections affects the velocities of high-frequency flexural waves more than low-frequency waves, and its effect is azimuthally dependent (Simsek and Sinha, 2008a, 2008b). This may alter the

cross-dipole flexural dispersion curves at high frequencies and result in a dispersion crossover when the formation exhibits HTI anisotropy.

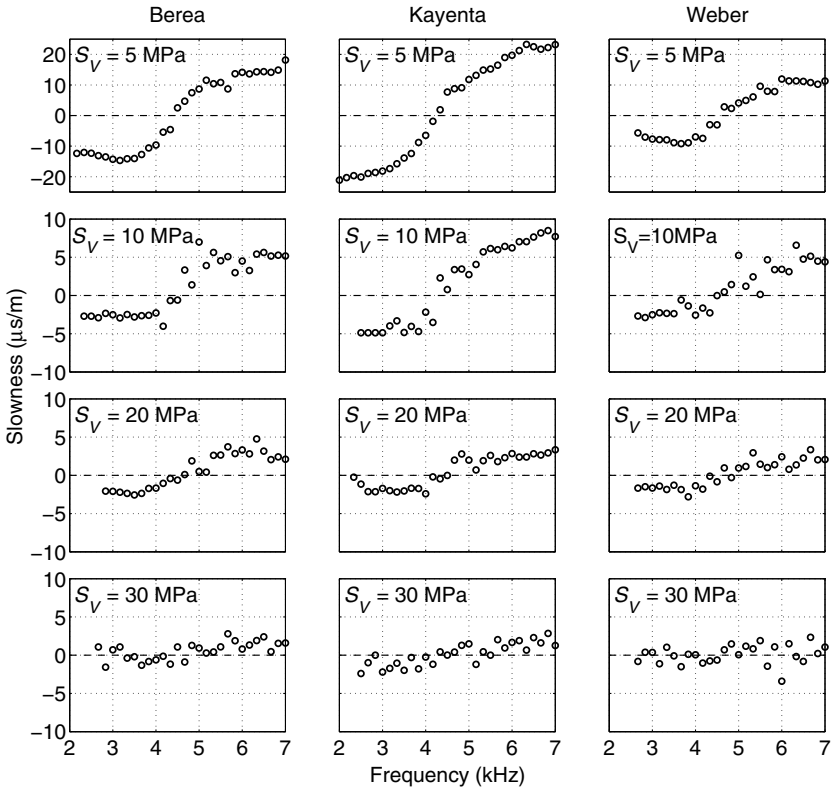

Figure 11. Difference of the flexural dispersion at the two azimuths shown in Figure 10. The dispersion difference is obtained by subtracting the dispersion at 90° (red circles in Figure 10) from that at 0° (black circles in Figure 10). Note different vertical scales.

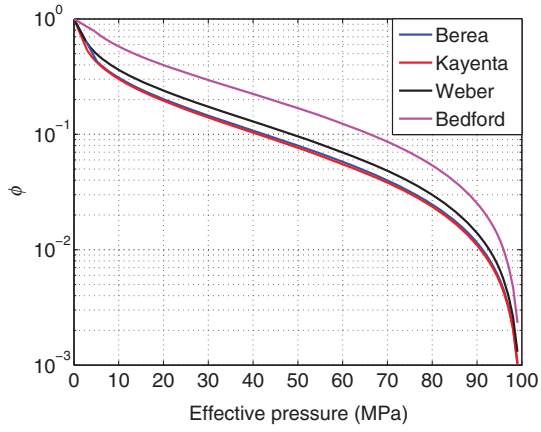

Figure 12. Compressible compliance percentage ϕ (equation 6) versus effective pressure for the four rock samples. In the calculation of ϕ using equation 6, $\mu_{\min}^{-1}$ and $\mu_{\max}^{-1}$ are the shear compliances at 100 and 0 MPa, respectively. For the Kayenta sandstone sample and the Bedford limestone sample, the maximum effective pressure of the data shown in Figure 1 is less than 100 MPa, and we use a logarithm function (Fang et al., 2013b) to fit the velocity data and then estimate the velocities at pressures beyond the maximum measured pressure from the fitting curve.

For simplicity in the modeling, we use an ellipse to represent an elongated noncircular borehole cross section. The borehole ellipticity is defined as

$$e = \frac{a_{\max}}{a_{\min}}, \tag{7}$$

where $a_{\max}$ and $a_{\min}$ are the borehole major and minor radii, respectively. Although finite-element methods (e.g., Jørgensen and Burns, 2013) or semianalytical perturbation methods (Simsek and Sinha, 2008a) may be more suitable for modeling elliptical boreholes, the finite-difference method used in our simulations can give the first-order effect of borehole ellipticity on flexural dispersion because the grid size (2.5 mm) is much smaller than the borehole diameter and the wavelength.

Because we are not considering the effect of stress on near-borehole anisotropy in this section, the formation rock type is not considered. We take the P- and S-wave velocities of the Berea sandstone sample at zero stress state as the horizontal P- and S-wave velocities of the HTI formation along the symmetry axis direction (i.e., the y-direction) and use selected anisotropic parameters ($\varepsilon = \gamma$, $\delta = 0$) to calculate the stiffness tensor of the formation. Figure 14a–14c shows the effects of an HTI formation on flexural dispersion of dipoles at 0° (black circles) and 90° (red circles) for anisotropies $\varepsilon = \gamma = 0.01$, $\varepsilon = \gamma = 0.02$, and $\varepsilon = \gamma = 0.05$, respectively, when the borehole is circular (i.e., $e = 1$). We assume that the borehole major axis is along the x-direction, and we vary $a_{\max}$ to obtain borehole models with different ellipticity while fixing $a_{\min}$ at 10 cm. Figure 14d–14f shows the effects of borehole ellipticity on flexural dispersion for $e = 1$, 1.1, and 1.2, respectively, when the formation is isotropic (i.e., $\varepsilon = \gamma = 0$). We can see that formation anisotropy has a larger influence on the low-frequency portions of the flexural dispersion while borehole ellipticity affects flexural dispersion more significantly at higher frequencies. When an elliptical borehole with the major axis along the x-direction is surrounded by an HTI formation with the symmetry axis along the y-direction, flexural waves in the x-direction are faster at low frequencies and they become slower at high frequencies compared with those in the y-direction. This results in a dispersion crossover, as shown in Figure 15. Figure 15a–15f shows the flexural dispersion for boreholes with ellipticity of $e = 1.1$ and 1.2, respectively,

Table 3. Stresses of three stress states with varying differential stress.

Model	S_V	S_H	S_h	$\Delta S_{\text{Diff}} = S_H - S_h$
a	30 MPa	35 MPa	25 MPa	10 MPa
b	30 MPa	35 MPa	20 MPa	15 MPa
c	30 MPa	35 MPa	15 MPa	20 MPa

when the formation exhibits different anisotropies. The two flexural dispersion curves clearly show a crossover even when $e = 1.1$ and $\varepsilon = \gamma = 0.01$. Figure 15c does not show a dispersion crossover because the formation anisotropy ($\varepsilon = \gamma = 0.05$) is strong enough to overwhelm the effect of borehole ellipticity ($e = 1.1$) in the studied frequency range and shift the crossover to a higher frequency beyond 7 kHz. When the borehole ellipticity increases to 1.2, as shown in Figure 15f, the dispersion crossover appears again in the studied frequency range. Comparing Figures 6, 11, and 15, we can see that the dispersion crossover caused by the combined effect of formation intrinsic anisotropy and borehole ellipticity can appear at a frequency ($4 \sim 5$ kHz) similar to that caused by stress-induced anisotropy. Figure 16 further shows that the borehole major axis does not have to be normal to the symmetry axis of the HTI formation to cause the flexural dispersion crossover. The elliptical borehole with $e = 1.2$ is rotated counterclockwise by 30°, as shown in Figure 16a, and the dipole orientations are kept at 0° and 90°. Figure 16b and 16c, respectively, shows the flexural dispersion for $\varepsilon = \gamma = 0.01$ and $\varepsilon = \gamma = 0.02$. The dispersion crossover can occur even though the borehole major axis is not orthogonal to the symmetry axis of the HTI formation.

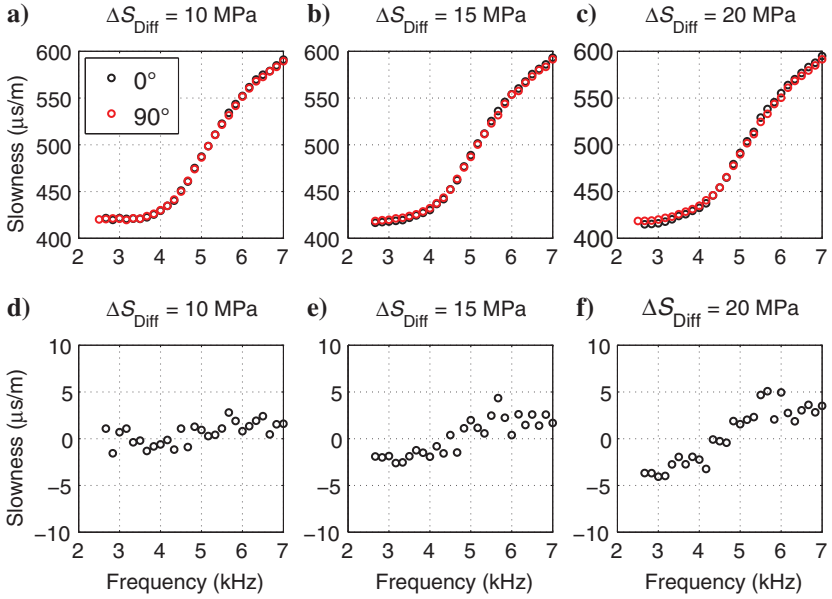

Figure 13. (a-c) Flexural dispersion for the Berea sandstone borehole model under the compression of different triaxial stresses with varying differential stress ΔS_{Diff} ($S_H - S_h$). Panels (d-f), respectively, show the corresponding differences of dispersion in panels (a-c). Table 3 lists the stress values for the three stress states. The black and red circles are, respectively, the dispersion along the x- and y-directions (0° and 90°, respectively).

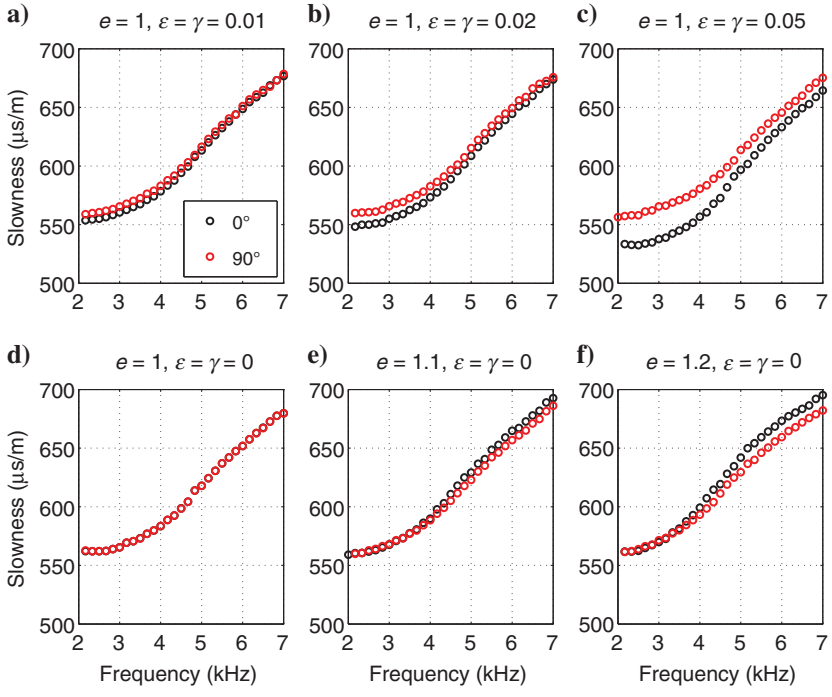

Figure 14. Panels (a-f) show the flexural dispersion for HTI ($\varepsilon = \gamma > 0$, $\delta = 0$) and isotropic ($\varepsilon = \gamma = \delta = 0$) models, respectively. The borehole is circular in the HTI models (a-c), and the borehole ellipticity e of the isotropic models (d-f) varies from 1 to 1.2. Black and red circles are, respectively the dispersion along the x- and y-directions (0° and 90°, respectively). The symmetry axis of the HTI formations is in the y-direction.

Figures 15 and 16 demonstrate that the combined effect of formation anisotropy and borehole ellipticity can result in the flexural dispersion crossover when the borehole elongation direction is in a close alignment with the fast direction of an anisotropic formation. If the borehole elongation direction is along the formation slow direction (i.e., the symmetry axis direction of the HTI formation), we would not see any crossover in the flexural dispersion. However, this is true only for fast formations. For slow formations, the result could be different because the shear velocity of a slow formation is smaller than the borehole fluid velocity. Figure 17 shows the simulation results for elliptical boreholes surrounded by slow anisotropic formations with different anisotropies. The borehole major axis direction is set to be parallel to the HTI formation symmetry direction (i.e., the y-direction). Table 4 gives the isotropic velocities and density of the rock used in the modeling. Figure 17b and 17f shows that the combination of HTI anisotropy and borehole ellipticity can cause a flexural dispersion crossover in slow formations when the borehole elongates in the slow direction of an HTI formation.

We have demonstrated here that flexural dispersion crossover can result not only from borehole stress-induced anisotropy but also from the combined effect of formation intrinsic anisotropy and borehole elongation. Flexural dispersion crossover is thus not always an indicator of borehole stress-induced anisotropy. This observation is consistent with earlier modeling results that dipole dispersion crossover is an indicator

of stress-induced anisotropy only in the presence of a circular borehole in a formation that is isotropic in the absence of stresses (Sinha and Kostek, 1996). A thorough and correct interpretation of the flexural dispersion crossover needs to take into account the effects of stress-induced and intrinsic anisotropies and borehole cross-sectional geometry.

DISCUSSION

Borehole stress-induced anisotropy versus formation intrinsic anisotropy and borehole ellipticity

Stress-induced anisotropy near a borehole drilled in a sedimentary rock environment is always present because the stiffness of most sedimentary rocks is stress-dependent. Formation intrinsic anisotropy caused by fine layers, aligned fractures, or microstructures found in shale is common in the earth, and we have shown that 1% intrinsic anisotropy is large enough to separate the flexural dispersion curves. Boreholes drilled in the earth are often noncircular. Sinha et al. (2000) find that the commonly encountered borehole ellipticity is around 1.25 in a limestone reservoir. Our modeling results indicate that a borehole ellipticity of 1.1 is large enough to separate the flexural dispersion curves at high frequencies, so the effect of borehole ellipticity is as important as stress-induced and intrinsic anisotropies. Therefore, borehole stress-induced anisotropy, formation intrinsic anisotropy, and borehole ellipticity are equally important in this problem. However, all existing approaches for modeling the effect of borehole stress-induced anisotropy on flexural wave propagation assume that the borehole is circular and do not consider the effect of preexisting intrinsic anisotropy in the rock. In our future work, we need to develop a method that can model the stress-dependent elasticity of anisotropic rocks to calculate the borehole stress-induced anisotropy when the formation is intrinsically anisotropic at the zero stress state.

General formation anisotropy

We have considered formation anisotropy in the form of HTI symmetry. When the symmetry axis of a transversely isotropic (TI) formation is not normal to the borehole axis, the borehole dipole response is expected to exhibit some degree of azimuthal dependence, as long as the symmetry axis is not parallel to the borehole axis. A general tilted transversely isotropic (TTI) formation can split flexural waves into fast and slow components (Sinha et al., 2006; He et al., 2010), and the separation of the dispersion of fast and slow flexural waves depends on the strength of anisotropy. If the formation exhibits more complicated anisotropy, for example, orthorhombic anisotropy, a detailed modeling study is needed to understand the borehole acoustic response.

Drilling-induced borehole breakouts and fractures

The method (Fang et al., 2013b) used in calculating the borehole stress-induced anisotropy in this study is purely elastic and neglects the effects of rock failure and stress-induced opening of fractures/cracks. In situ, the horizontal principal stresses generally satisfy $S_H < 3S_h$ (Zoback et al., 1985), so there is no tensile stress on the wellbore for vertical wells because the hoop stress (equation 1) is compressive at all azimuths. However, tensile stress around a borehole may still appear in high pore pressure zones or when

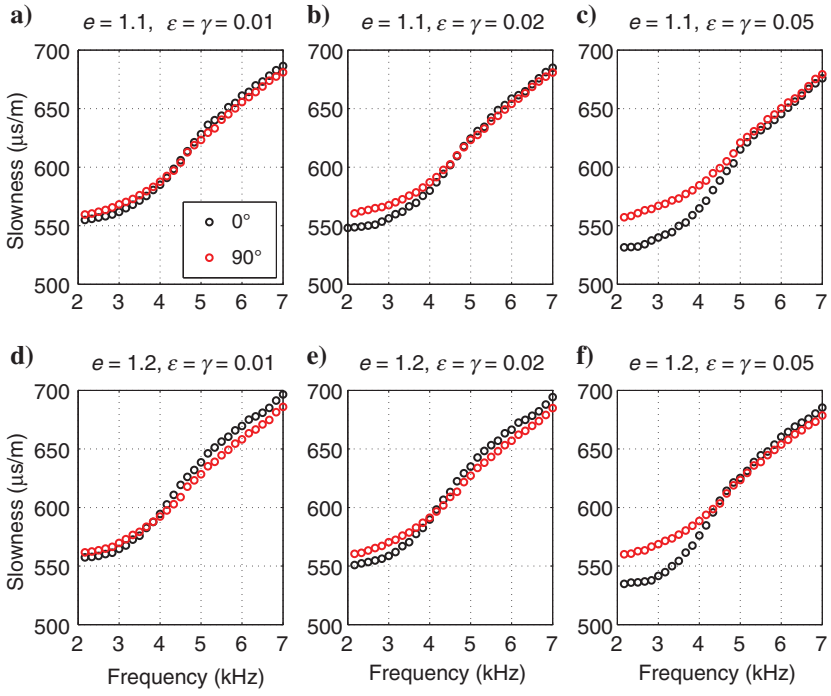

Figure 15. Panels (a-f) show the flexural dispersion for models with different anisotropies ($\varepsilon = \gamma > 0$, $\delta = 0$) and different borehole ellipticity ($e > 1$). The black and red circles are, respectively, the dispersion along the x- and y-directions (0° and 90°, respectively). The symmetry axis of the HTI formations is in the y-direction. The borehole major axis is along the x-direction.

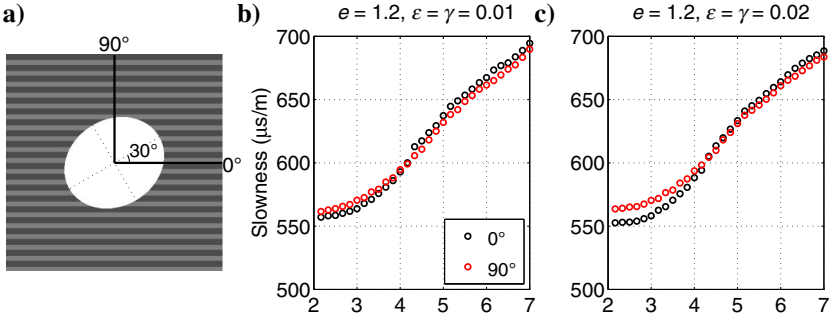

Figure 16. (a) Schematic showing a borehole with ellipticity of $e = 1.2$ and major axis 30° to the x-axis in an HTI formation with the symmetry axis in the y-direction. (b and c) Flexural dispersion for two models with different anisotropies.

the borehole mud pressure is significantly large or in horizontal wells when the overburden stress is much larger than the horizontal stresses. Borehole tensile stress may cause tensile failure at the wellbore along the direction of the maximum principal stress in the borehole cross-sectional plane and induce fractures. Similar to the influence of borehole breakouts, Zheng et al. (2009, 2010) and Lei and Sinha (2013) show that drilling-induced fractures can also split the flexural wave into fast and slow components. The fast and slow flexural wave dispersion curves behave differently at different frequencies depending on the fracture length, orientation, width, and infill properties (Zheng et al., 2009, 2010; Lei and Sinha, 2013).

When a formation is intrinsically anisotropic and the anisotropy is caused by natural fractures that are generally aligned with the S_H direction, there are several possible field conditions. When there is an absence of drilling-induced wellbore fractures, a breakout can cause a crossover in flexural dispersion only in a slow formation (Figure 17) because the breakout direction is along the formation anisotropy symmetry direction. Zheng et al. (2009) show that a shallow (~3 cm deep from wellbore) fluid-filled fracture splits flexural dispersion at high frequencies whereas it has little effect at low frequencies, which is similar to the influence of breakouts as shown in Figure 14e and 14f. Because drilling-induced fractures occur at an angle of 90° apart from the breakouts along a borehole, they may lead to a dispersion crossover in a fast formation with intrinsic anisotropy. However, this needs to be further investigated for specific fracture geometry and formation anisotropy. When a borehole has breakouts and drilling-induced fractures, we have to determine the borehole flexural wave response through simulations for given wellbore conditions. If a drilling-induced fracture is solid filled, the corresponding borehole flexural wave response could be different from that of a fluid-filled fracture because of the nonzero shear modulus of the fracture infill (Zheng et al., 2010). The influence of drilling-induced fractures is not investigated in this paper, a further modeling study is necessary to investigate the actual response for a specific field condition.

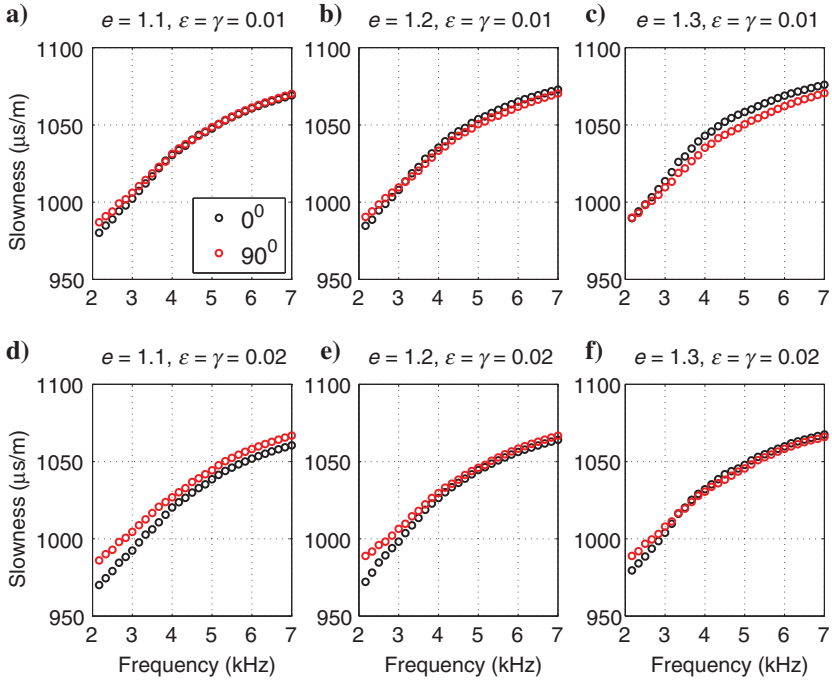

Figure 17. Flexural dispersion for slow formation models with different anisotropies ($\varepsilon = \gamma > 0$, $\delta = 0$) and different borehole ellipticity e. The black and red circles are, respectively, the dispersion along the x- and y-directions (0° and 90°, respectively). The HTI formation symmetry axis and the borehole major axis are along the y-direction.

Table 4. Properties of a slow formation (Yang et al., 2011).

V_P	V_S	Density
2478 m/s	1016 m/s	2270 kg/m^3

Other factors could affect the result

Besides elasticity anisotropy, borehole geometry, and drilling-induced rock failure, the plastic yielding of the near-wellbore formation, tool eccentricity, drilling fluid invasion, and other complicated near-wellbore field situations could also affect the flexural wave behavior. The use of all available logging data, such as multiarm caliper data, ultrasonic data, resistivity logs, gamma-ray logs, and other lithology logs, may lead to a more reliable interpretation of field data.

CONCLUSIONS

We have shown that the flexural dispersion crossover can be caused either by borehole stress-induced anisotropy or by the combined effect of formation intrinsic anisotropy and borehole elongation. When a borehole is subjected to triaxial stress compression in the earth, the flexural dispersion crossover caused by borehole stress-induced anisotropy is detectable only when the formation is sufficiently compliant, which generally requires that the overburden stress S_V is small (<10 MPa). This indicates that borehole stress-induced anisotropy is possibly the cause of flexural dispersion crossover only in the shallow subsurface or in high pore pressure zones, where the effective confining pressure is small. However, the flexural dispersion crossover caused by the combined influence of formation intrinsic anisotropy and borehole elongation can occur at any depth when the formation anisotropy and borehole ellipticity meet a certain criterion, which is not hard to satisfy because a small change in borehole ellipticity (~1.1) and very weak anisotropy (~1%) are enough to generate the dispersion crossover. Our modeling results show that stress-induced anisotropy, formation intrinsic anisotropy, and borehole ellipticity all have a first-order effect on flexural dispersion. Therefore, we have to consider the total effect of these three factors to obtain a correct interpretation when we encounter a crossover in cross-dipole flexural dispersion.

ACKNOWLEDGMENTS

We are grateful to the assistant editor J. Shragge, R. Song, and two anonymous reviewers for their constructive comments. We thank T. Chen and D. Burns for helpful discussion about sonic logging. X. Fang was sponsored by a Halliburton postdoctoral fellowship.

APPENDIX A

BOREHOLE ELLIPTICITY CAUSED BY WELLBORE ELASTIC DEFORMATION UNDER STRESS

We will analytically calculate the borehole ellipticity that is caused by the elastic deformation of the wellbore due to the presence of anisotropic stresses. When stresses are applied on a rock containing a circular borehole that was drilled prior to the imposition of stresses, the radial displacement at the wellbore where $r = a$ (a: borehole radius) is given as (Amadei, 1983)

$$\Delta u_r(\theta) = (S_H + S_h)\frac{a}{E} + (S_H - S_h)\frac{2a(1-\nu^2)}{E} \times \cos 2\theta - \frac{a\nu}{E}S_V, \quad \text{(A-1)}$$

where E and ν are, respectively, the Young's modulus and Poisson's ratio; S_H, S_h, and S_V are the principal stresses as shown in Figure 2; and θ is measured from the S_H direction.

As shown in Figure A-1, the radial displacement Δu_r can be separated into two parts: (1) elastic deformation of the intact formation without the borehole at positions where $r = a$ (Figure A-1b) and (2) elastic deformation due to the borehole boundary (Figure A-1c). When there is no borehole, the radial displacement of an intact formation at the circle $r = a$ is (Amadei, 1983)

$$\Delta u_r^0(\theta) = (S_H + S_h)\frac{a(1-\nu)}{2E} + (S_H - S_h)\frac{a(1+\nu)}{2E} \times \cos 2\theta - \frac{a\nu}{E}S_V. \quad \text{(A-2)}$$

In the earth, in situ stresses are present before drilling, so the actual wellbore deformation caused by the redistribution of the stresses around a borehole after the drilling is

$$\Delta u_r^i(\theta) = \Delta u_r(\theta) - \Delta u_r^0(\theta) = (S_H + S_h)\frac{a(1+\nu)}{2E} + (S_H - S_h)\frac{a(1+\nu)(3-4\nu)}{2E}\cos 2\theta, \quad \text{(A-3)}$$

where Δu_r^0 is the displacement of the formation caused by tectonic stresses before drilling the borehole and Δu_r^i is the displacement at the wellbore caused by drilling-induced stress changes.

Because the two horizontal principal stresses are defined along $\theta = 0^\circ$ and 90°, the borehole ellipticity is given as

$$e = \frac{a + \Delta u_r^i(0^o)}{a + \Delta u_r^i(90^o)} = \frac{1 + \Delta S_{\text{Diff}}(1+\nu)(3-4\nu)/(2E)}{1 - \Delta S_{\text{Diff}}(1+\nu)(3-4\nu)/(2E)}, \quad \text{(A-4)}$$

where the differential stress $\Delta S_{\text{Diff}} = S_H - S_h$.

For Poisson's medium $\nu = 0.25$, we have

$$e = \frac{1 - 1.25\Delta S_{\text{Diff}}/E}{1 + 1.25\Delta S_{\text{Diff}}/E} \approx 1 - 2.5\frac{\Delta S_{\text{Diff}}}{E}. \quad \text{(A-5)}$$

At a nominal depth at which oil or gas exploration occurs, E of a sedimentary rock is usually on the order of 10 GPa and ΔS_{Diff} is on the order of 10 MPa; thus, $\Delta S_{\text{Diff}}/E \sim 0.001$ and e is on the order of 1.001. Figure A-2 shows the borehole ellipticity calculated from

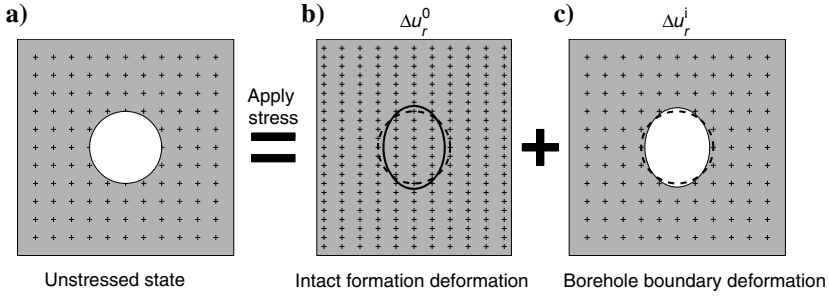

Figure A-1. (a) Schematic showing a circular borehole in a homogeneous medium before stress is applied; panels (b and c) illustrate the displacements at $r = a$ caused by formation deformation (equation A-2) and borehole boundary (equation A-3), respectively. Dashed circles in panels (b and c) represent the position of the circular wellbore before deformation. The solid ellipse in panel (b) schematically indicates the change of the dashed circle after formation deformation.

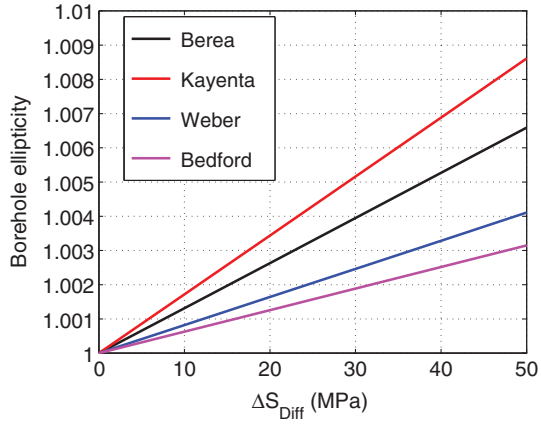

Figure A-2. Borehole ellipticity (equation A-5) caused by wellbore elastic deformation due to borehole stress redistribution. The E and ν of each rock sample are taken as their values at the zero stress state.

equation A-4 for the four rock samples under different differential stresses. We can see that e is generally very small. Therefore, borehole ellipticity caused by wellbore elastic deformation due to borehole stress redistribution can be neglected because it is much smaller than that caused by other factors, such as borehole breakouts.

REFERENCES

Amadei, B., 1983, Rock anisotropy and the theory of stress measurements: Springer Verlag.

Brown, S., and A. Cheng, 2007, Velocity anisotropy and heterogeneity around a borehole: 77th Annual International Meeting, SEG, Expanded Abstracts, 318–322.

Cheng, N. Y., C. H. Cheng, and M. N. Toksöz, 1995, Borehole wave propagation in three dimensions: Journal of the Acoustical Society of America, **97**, 3483–3493, doi: 10.1121/1.412996.

Coyner, K. B., 1984, Effects of stress, pore pressure, and pore fluids on bulk strain, velocity, and permeability in rocks: Ph.D. thesis, Massachusetts Institute of Technology.

Fang, X. D., C. Chang, and A. Cheng, 2013a, System and method for determining shear wave anisotropy in a vertically transversely isotropic formation: U.S. Patent 2,013,022,421.

Fang, X. D., and M. C. Fehler, 2014a, Does dipole dispersion crossover indicate borehole stress-induced anisotropy?: 76th Annual International Conference and Exhibition, EAGE, Expanded Abstract, We D203 15.

Fang, X. D., and M. C. Fehler, 2014b, Numerical investigation of borehole dipole flexural dispersion crossover under triaxial stress: 84th Annual International Meeting, SEG, Expanded Abstracts, 606–611.

Fang, X. D., M. C. Fehler, and A. Cheng, 2014, Simulation of the effect of stress-induced anisotropy on borehole compressional wave propagation: Geophysics, **79**, no. 4, D205–D216, doi: 10.1190/geo2013-0186.1.

Fang, X. D., M. C. Fehler, Z. Y. Zhu, T. R. Chen, S. Brown, A. Cheng, and M. N. Toksöz, 2013b, An approach for predicting stress-induced anisotropy around a borehole: Geophysics, **78**, no. 3, D143–D150, doi: 10.1190/geo2012-0145.1.

Gaede, O., F. Karpfinger, J. Jocker, and R. Prioul, 2012, Comparison between analytical and 3D finite element solutions for borehole stresses in anisotropic elastic rock: International Journal of Rock Mechanics and Mining Sciences, **51**, 53–63, doi: 10.1016/j.ijrmms.2011.12.010.

He, X., H. Hu, and W. Guan, 2010, Fast and slow flexural waves in a deviated borehole in homogeneous and layered anisotropic formations: Geophysical Journal International, **181**, 417–426, doi: 10.1111/j.1365-246X.2010.04503.x.

Jaeger, J. C., N. G. W. Cook, and R. W. Zimmerman, 2007, Fundamentals of rock mechanics: Blackwell Publishing.

Jørgensen, O., and D. Burns, 2013, Novel finite-element approach applied to borehole quadrupole dispersion analysis in stress-sensitive formations: Geophysics, **78**, no. 6, D499–D509, doi: 10.1190/geo2012-0487.1.

Lei, T., and B. K. Sinha, 2013, Fracture-induced anisotropy and reflectivity of elastic waves in a fluid-filled borehole: 83rd Annual International Meeting, SEG, Expanded Abstracts, 504–508.

Liu, Q. H., and B. K. Sinha, 2000, Multipole acoustic waveforms in fluid-filled boreholes in biaxially stressed formations: A finite-difference method: Geophysics, **65**, 190–201, doi: 10.1190/1.1444710.

Liu, Q. H., and B. K. Sinha, 2003, A 3D cylindrical PML/FDTD method for elastic waves in fluid-filled pressurized boreholes in triaxially stressed formations: Geophysics, **68**, 1731–1743, doi: 10.1190/1.1620646.

Mao, N. H., 1987, Shear wave transducer for stress measurements in boreholes: U.S. Patent 4,641,520.

Mavko, G., T. Mukerji, and N. Godfrey, 1995, Predicting stress-induced velocity anisotropy in rocks: Geophysics, **60**, 1081–1087, doi: 10.1190/1.1443836.

Oda, M., T. Yamabe, and K. Kamemura, 1986, A crack tensor and its relation to wave velocity anisotropy in jointed rock masses: International Journal of Rock Mechanics and Mining Sciences and Geomechanics Abstracts, **23**, 387–397, doi: 10.1016/0148-9062(86)92304-1.

Rao, R., and M. N. Toksöz, 2005, Dispersive wave analysis — Method and applications: Annual report of borehole acoustics and logging and reservoir delineation consortia, Massachusetts Institute of Technology.

Sayers, C. M., 2005, Sensitivity of elastic-wave velocities to stress changes in sandstones: The Leading Edge, **24**, 1262–1266, doi: 10.1190/1.2149646.

Sayers, C. M., 2007, Effects of borehole stress concentration on elastic wave velocities in sandstones: International Journal of Rock Mechanics and Mining Sciences and Geomechanics Abstracts, **44**, 1045–1052, doi: 10.1016/j.ijrmms.2007.04.002.

Sayers, C. M., J. Adachi, and A. D. Taleghani, 2008, The effect of near-wellbore yield on elastic wave velocities in sandstones: 78th Annual International Meeting, SEG, Expanded Abstracts, 339–343.

Sayers, C. M., S. Kisra, K. Tagbor, A. D. Taleghani, and J. Adachi, 2007, Calibrating the mechanical properties and in-situ stresses using acoustic radial profiles: Presented at Society of Petroleum Engineers Annual Technical Conference and Exhibition, SPE-110089-MS.

Simsek, E., and B. K. Sinha, 2008a, Analysis of noncircular fluid-filled boreholes in elastic formations using a perturbation model: Journal of the Acoustical Society of America, **124**, 213–217, doi: 10.1121/1.2931954.

Simsek, E., and B. K. Sinha, 2008b, Estimation of borehole ellipticity using cross-dipole dispersions: 78th Annual International Meeting, SEG, Expanded Abstracts, 329–333.

Simsek, E., B. K. Sinha, and S. Zeroug, 2007, Influence of breakouts on borehole sonic dispersions: 77th Annual International Meeting, SEG, Expanded Abstracts, 313–317.

Sinha, B. K., 2001, Stress-induced changes in the borehole Stoneley and flexural dispersions: 71st Annual International Meeting, SEG, Expanded Abstracts, 337–340.

Sinha, B. K., M. R. Kane, and B. Frignet, 2000, Dipole dispersion crossover and sonic logs in a limestone reservoir: Geophysics, **65**, 390–407, doi: 10.1190/1.1444734.

Sinha, B. K., and S. Kostek, 1995, Identification of stress induced anisotropy in formations: U.S. Patent 5,398,215.

Sinha, B. K., and S. Kostek, 1996, Stress-induced azimuthal anisotropy in borehole flexural waves: Geophysics, **61**, 1899–1907, doi: 10.1190/1.1444105.

Sinha, B. K., and Q. H. Liu, 2002, Acoustic waves in pressurized boreholes in formation with triaxial stresses, *in* Yuhas, M. P., ed., 2002 IEEE Ultrasonics Symposium Proceedings, vol. 1, IEEE, 505–510 .

Sinha, B. K., and Q. H. Liu, 2004, Elastic waves in deviated boreholes in formations with triaxial stresses: *in* Yuhas, M. P., ed., 2004 IEEE Ultrasonics Symposium Proceedings, vol. 1, IEEE, 525–528.

Sinha, B. K., T. J. Plona, K. W. Winkler, and R. M. D'Angelo, 1995, Stress-induced dipole anisotropy in a dry Berea sandstone: 65th Annual International Meeting, SEG, Expanded Abstracts, 22–25.

Sinha, B. K., E. Simsek, and Q. H. Liu, 2006, Elastic-wave propagation in deviated wells in anisotropic formations: Geophysics, **71**, no. 6, D191–D202, doi: 10.1190/1.2358402.

Tang, X. M., and C. Cheng, 2004, Quantitative borehole acoustic methods: Elsevier.

Tang, X. M., N. Y. Cheng, and A. Cheng, 1999, Identifying and estimating formation stress from borehole monopole and cross-dipole acoustic measurement: Presented at Society of Petrophysicists and Well-Log Analysts 40th Annual Logging Symposium, SPWLA-1999-QQ.

Tang, X. M., T. Wang, and D. Patterson, 2002, Multipole acoustic logging-while-drilling: 72nd Annual International Meeting, SEG, Expanded Abstracts, 364–367.

Winkler, K. W., 1996, Azimuthal velocity variations caused by borehole stress concentrations: Journal of Geophysical Research, **101**, 8615–8621, doi: 10.1029/96JB00093.

Winkler, K. W., B. K. Sinha, and T. J. Plona, 1998, Effects of borehole stress concentrations on dipole anisotropy measurements: Geophysics, **63**, 11–17, doi: 10.1190/1.1444303.

Yang, J., B. K. Sinha, and T. M. Habashy, 2011, Estimation of formation shear and borehole-fluid slowness using sonic dispersion data in well-bounded cased boreholes: Geophysics, **76**, no. 6, E187–E197, doi: 10.1190/geo2010-0413.1.

Zheng, Y., X. Tang, and D. J. Patterson, 2009, Borehole acoustic dipole response with drilling-induced vertical fractures: 79th Annual International Meeting, SEG, Expanded Abstracts, 356–360.

Zheng, Y., X. Tang, and D. J. Patterson, 2010, Borehole flexural-wave response to vertical solid-filled fractures: 80th Annual International Meeting, SEG, Expanded Abstracts, 563–567.

Zoback, M. D., 2010, Reservoir geomechanics: Cambridge University Press.

Zoback, M. D., D. Moos, L. Mastin, and R. N. Anderson, 1985, Well bore breakouts and in situ stress: Journal of Geophysical Research, **90**, 5523–5530, doi: 10.1029/JB090iB07p05523.